Electrochimica Acta 259 (2018) 647–654

Contents lists available at ScienceDirect

Electrochimica Acta

journal homepage: www.elsevier.com/locate/electacta

Flexible free-standing $Na_4Mn_9O_{18}$/reduced graphene oxide composite film as a cathode for sodium rechargeable hybrid aqueous battery

Guanghui Yuan [a], Jiming Xiang [a], Huafeng Jin [a], Yanzi Jin [a], Lizhou Wu [a], Yongguang Zhang [b, **], Almagul Mentbayeva [c, d], Zhumabay Bakenov [c, d, *]

[a] Department of Chemistry and Chemical Engineering, Ankang University, Shaanxi, Ankang 725000, China
[b] Synergy Innovation Institute of GDUT, Heyuan, Guangdong Province, China
[c] Institute of Batteries LLC, 53 Kabanbay Batyr Avenue, Astana 010000, Kazakhstan
[d] Department of Chemical Engineering, National Laboratory Astana, Nazarbayev University, 53 Kabanbay Batyr Avenue, Astana 010000, Kazakhstan

ARTICLE INFO

Article history:
Received 13 July 2017
Received in revised form
20 October 2017
Accepted 2 November 2017
Available online 4 November 2017

Keywords:
$Na_4Mn_9O_{18}$/reduced graphene oxide
Free-standing electrode
Composite film
Cathode material
Rechargeable hybrid aqueous battery

ABSTRACT

A novel free-standing $Na_4Mn_9O_{18}$/reduced graphene oxide (NMO-RGO) composite was successfully prepared by a facile vacuum filtration technique. Scanning and transmission electron microscopy studies revealed formation of a film with needle-like $Na_4Mn_9O_{18}$ homogeneously distributed and anchored on the RGO matrix. A sodium rechargeable hybrid aqueous battery with this novel cathode and zinc anode was first investigated and reported. The NMO-RGO film delivered a reversible discharge capacity of about 83 mAh g^{-1} when cycled galvanostatically at a current density of 0.1 A g^{-1}, which was for about 78% higher than that of $Na_4Mn_9O_{18}$ prepared by a slurry casting technique. This significant enhancement of electrochemical properties of NMO-RGO was due to the presence of graphene sheets in this free-standing composite cathode. These sheets form an agile substrate with a high conductivity to guarantee a successive electronic conduction channels in the electrode. In the same time, such composition and structure enables accommodation of the volume changes of $Na_4Mn_9O_{18}$ during sodium insertion-extraction.

1. Introduction

A tremendous progress in electronic devices, electric transport and implementation of renewable energy has strongly motivated and demanded the development of next generation high performance rechargeable batteries [1,2]. Lithium-ion batteries (LIBs) are leading the market for such systems. However, there are some limitations of LIBs such as high cost and limited resources of lithium and other components, and safety concerns arising from the use of organic flammable electrolytes, which restrict their application in large-scale storage system for renewable energy and electric vehicles [3]. Considering the similarities in properties of lithium and sodium, and low cost and abundance of the latter, sodium-ion batteries are considered as a very strong alternative to lithium-ion cells, especially, due to their high potential for energy accumulation in large scales [4,5]. On the other hand, recently a remarkable attention has been paid to lithium-ion aqueous rechargeable batteries such as ReHABs (rechargeable hybrid aqueous batteries) due to use of aqueous electrolytes instead of flammable organic solutions, which own many virtues such as low-toxicity, low cost and excellent safety [6–10]. Recently, sodium-based batteries with an aqueous electrolyte using sodium birnessite Na_xMnO_2 ($x = 0.70, 0.44$ or 0.95) as a cathode, activated carbon, $NaV_3(PO_4)_3$@C nanofiber or zinc as an anode have been reported [11–13]. However, most of these batteries suffer from poor performance and not yet able to compete with LIBs. Therefore, the further studies on improvement of electrochemical properties of the mentioned and other sodium compounds that can be used in sodium-based batteries, and exploring new sodium-based electrode materials, which possess high capacity, is required. Along with other important characteristics, electronic conductivity and Na^+ ion diffusion rate are not yet satisfactorily in the sodium

* Corresponding author. Institute of Batteries, Department of Chemical Engineering, National Laboratory Astana, Nazarbayev University, 53 Kabanbay Batyr Avenue, Astana 010000, Kazakhstan.
** Corresponding author. Synergy Innovation Institute of GDUT, Heyuan, Guangdong Province, China.
E-mail addresses: zyg1984723@hotmail.com (Y. Zhang), zbakenov@nu.edu.kz (Z. Bakenov).

https://doi.org/10.1016/j.electacta.2017.11.015

compounds, which results in a low rate capability [14,15]. Carbon materials such as graphene and reduced graphene oxide (RGO) have been demonstrated as promising conductive additives to electrode materials for ReHABs as well as for LIBs due to their excellent electrochemical stabilities, high specific surface area and outstanding electronic transport properties [16–20].

Recently, development of light (high energy density), high performance and binder-free electrodes for rechargeable batteries to power new applications including light electric/hybrid vehicles and soft portable electronic devices has been accelerated [21–23]. Some flexible films have been developed as electrodes for high performance lithium-ion batteries [24–26]. However, to best of our knowledge there are very few work reported [12] on flexible film electrodes for aqueous electrolyte batteries, both lithium and sodium based.

In this work, we designed and prepared a free-standing $Na_4Mn_9O_{18}$/Reduced Graphene Oxide (NMO-RGO) hybrid flexible film via a facile vacuum filtration method, and first investigated it as a cathode for sodium ReHAB. The use of this flexible NMO-RGO hybrid film as the electrode increases the specific capacity of a battery as well as simplifies its manufacturing and decreases the cost of the electrode due to eliminating the necessities of using current collector, conductive additive and binder. In the free-standing NMO-RGO film prepared in this work, 3D architecture is formed by the electrochemically active $Na_4Mn_9O_{18}$ needles densely anchored on a conductive matrix of graphene sheets. The network, interlaced by wrinkled graphene sheets, provides fast electron conduction paths and structural stability to the composite to mitigate the mechanical stresses developed upon sodium insertion-extraction process. Electrochemical results confirm that the NMO-RGO hybrid film exhibits a remarkably enhanced rate capability and stable cycling performance compared with $Na_4Mn_9O_{18}$ prepared by a slurry casting technique.

2. Experimental

2.1. Materials preparation

An improved Hummers' method was employed to synthesize graphene oxide (GO) from natural flake graphite (99%; Beijing DK Nanotechnology Co., Ltd. Product) [27]. Uniform GO suspension was prepared by dispersing 30 mg GO in 10 ml deionized (DI) water and ultrasound treatment of this suspension for 2 h, which resulted in brown GO suspension.

A facile hydrothermal method was used to prepare the $Na_4Mn_9O_{18}$ particles. Typically, 1.5 mmol Mn_2O_3 (99%; Tianjin Hengxing Chemical Preparation Co., Ltd.) was added dropwise into 30 ml of 5 mol dm^{-3} NaOH (99%; Tianjin Hengxing Chemical Preparation Co., Ltd.) aqueous solution and then the mixture was stirred vigorously. Further, the resulting suspension was poured into a 50 ml Teflon® autoclave, which was sealed and put into a furnace for 48 h at 220 °C, and then naturally cooled to room temperature. A precipitate was separated from the solution by centrifugation. Finally, the product was washed by DI water and ethanol (99%; Chongqing Chuandong Chemical (Group) Co., Ltd.) repeatedly to remove NaOH, and dried in a vacuum oven at 80 °C for 10 h.

An ordinary filtration method and a thermal reduction were employed to manufacture a free-standing NMO-RGO hybrid film. Typically, 20 mg $Na_4Mn_9O_{18}$ powder was dispersed into 10 ml as-prepared brown GO suspension. After ultrasonic treatment for 2 h, a suspension was filtered through a filter membrane (Millipore, 50 mm, 0.22 μm pore size) under a reduced pressure. The membrane with deposited film was washed with DI water, dried in air and immersed in acetone (99%; Chongqing Chuandong Chemical (Group) Co., Ltd.) for a few minutes. Then the film sample was peeled off from the membrane. In order to prepare a free-standing NMO-RGO hybrid film, the sample was heat treated at 220 °C for 2 h in air. The resulting free-standing flexible and bendable film was labeled as NMO-RGO-1. For comparison purposes, two more free-standing film samples were prepared as well by the same procedure using 15 mg and 10 mg $Na_4Mn_9O_{18}$. The resulting flexible and bendable films were labeled as NMO-RGO-2 and NMO-RGO-3, respectively. The complete preparation process is schematically illustrated in Scheme 1. All NMO-RGO samples prepared according to Scheme 1 were flexible self-standing films.

2.2. Material characterization

The X-ray diffraction (XRD) patterns of the samples were recorded using a Bruker D8 ADVANCE X-ray powder diffractometer using *Cu Kα* radiation ($\lambda = 0.15418$ nm) at a scanning rate of 0.02 s^{-1} in the 2θ range from 10 to 70°. Determination of the graphene content in the hybrid films was performed by thermal gravimetric analysis (TGA) (DSC–TGA; SDT Q600, TA Instruments Inc.) in air at a scanning rate of 10 °C min^{-1}. The specific surface areas and pore volumes of the synthesized samples were determined using nitrogen adsorption via Brunauer–Emmett–Teller (BET) and Barrett–Joyner–Halenda (BJH) methods. Scanning electron microscopy (SEM) images were obtained using an environmental scanning electron microscope with field emission gun (ESEM-FEG, Quanta FEG 400, FEI Inc.). Transmission electron microscopy (TEM) images were obtained on Tecnai G^2 F20 S-TWIN (FEI Inc.) instrument.

2.3. Electrochemical measurements

Swagelok®-type cells were used to execute electrochemical tests. The cell consisted of a zinc anode and a $Na_4Mn_9O_{18}$-based cathode. For comparison purposes, a $Na_4Mn_9O_{18}$ cathode was prepared by casting a slurry consisting of $Na_4Mn_9O_{18}$, acetylene black (99%, Shanghai Oujin Lithium Industrial Co., Ltd.) and polyvinylidene fluoride (99%, Shanghai Oujin Lithium Industrial Co., Ltd.) with 75:15:10 wt% in *N*-methyl-2-pyrrolidinone (99%, Shanghai Oujin Lithium Industrial Co., Ltd.) on stainless steel foil circles with a diameter of 10 mm, and vacuum drying at 110 °C for 10 h. The electrode was further pressed at 15 MPa pressure to ensure a good contact of the cathode films with the stainless steel current collector.

The freestanding NMO-RGO electrodes were prepared by cutting the films, obtained by the filtration method above, into circles with a diameter of 10 mm. Zinc sheets (99%, Shanghai Oujin Lithium Industrial Co., Ltd.) with thickness of 1 mm were cut into 10 mm circular sheets to be used as counter electrodes. Aqueous solution of 0.5 M $Zn(CH_3COO)_2$ (99%; Tianjin Hengxing Chemical Preparation Co., Ltd.) and 0.5 M $NaCH_3COO$ (99%; Tianjin Hengxing Chemical Preparation Co., Ltd.) was used as an electrolyte in all electrochemical cells. Absorbent glass mat (AGM) was used as a separator. Arbin SCTS 4000 (Arbin Instruments) and LAND (Wuhan LAND electronics Co.) battery testers were acquired to carry out galvanostatic charge-discharge tests within a cut off potentials of 1.05–1.85 V *vs.* Zn^{2+}/Zn. The galvanostat/potentiostat VMP3 (Bio-Logic Inc.) was used to conduct cyclic voltammetry (CV) at 0.1 mV s^{-1} in 1.0–1.95 V *vs.* Zn^{2+}/Zn and electrochemical impedance spectroscopy (EIS) at a frequency range of 0.01 Hz–100 kHz.

3. Results and discussion

The XRD patterns of graphene, NMO and NMO-RGO composites with different composition are shown in Fig. 1a. There are two

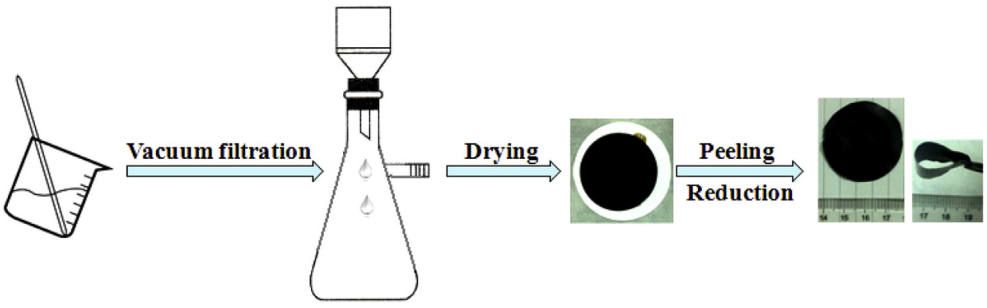

Scheme 1. Schematics of the NMO-RGO composite synthesis.

obvious diffraction peaks present in the patterns of pure graphene: a lower intensity peak at around 44.5° and a high intensity one at around 26.2°. These two peaks can be respectively attributed to the carbon (100) and (002) planes. The diffraction peaks at around 16.6°, 19.5°, 32.5°, 34.1° and 37.4° of NMO fit with the (140), (200), (340), (350) and (201) crystal planes of orthorhombic $Na_4Mn_9O_{18}$ according to the reference data (JCPDS #27-0750). The XRD patterns of NMO-RGO-1, NMO-RGO-2 and NMO-RGO-3 composites clearly exhibit the characteristic features of orthorhombic $Na_4Mn_9O_{18}$, indicating absence of phase transformation of NMO due to addition of graphene oxide. Furthermore, the intensity of a broad peak at around 26°, which is a typical signal of graphene, increases for the composites from NMO-RGO-1 to NMO-RGO-2 and further to NMO-RGO-3 reflecting an increase of the graphene content in this row. The XRD data confirm that the original graphene oxide was fully reduced into graphene during the hydrothermal process. The graphene content in these NMO-RGO composites was estimated using TGA analysis in air. The results presented in Fig. 1b show that a one-step weight loss occurs in all composites between 300 °C and 500 °C, which is due to combustion of graphene in air. When the temperature increases from 450 °C to 600 °C, the NMO-RGO-1, NMO-RGO-2 and NMO-RGO-3 composites maintain their weights almost unchanged, and these data allows estimating the graphene content in these samples as 51, 60 and 70 wt%, respectively.

The results of BET specific surface area and pore size distribution of the RGO and NMO-RGO composites are shown in Fig. 1c. From the adsorption branch of the isotherm, the BET specific surface areas of NMO-RGO-1, NMO-RGO-2 and NMO-RGO-3 composites are 47.4 $cm^2\ g^{-1}$, 68.3 $cm^2\ g^{-1}$ and 42.6 $cm^2\ g^{-1}$, respectively. These values for the composite films are higher than that obtained for the pristine RGO film, which exhibits a specific surface area of 31.5 $cm^2\ g^{-1}$. These results can be explained by intercalation of NMO particles into the layers of RGO. The NMO particles within the RGO sheets can prevent the graphene oxide nanosheets aggregation during the hydrothermal reduction process. On the other hand, NMO has much higher density than the RGO matrix. Excessive increasing of the NMO content could decrease the specific surface area of the NMO-RGO composite film. Therefore, the NMO-RGO-2 composite film having moderate NMO content shows the highest specific surface area of 68.3 $cm^2\ g^{-1}$. The total pore volumes of NMO-RGO-1, NMO-RGO-2, NMO-RGO-3 composites and RGO are 0.24 $cm^3\ g^{-1}$, 0.33 $cm^3\ g^{-1}$, 0.21 $cm^3\ g^{-1}$ and 0.19 $cm^3\ g^{-1}$, respectively. The relatively large specific surface area and pore volume provided by NMO-RGO-2 composite film would increase the contact area of electrolyte/electrode, which is beneficial for decreasing the areal current density when the composites are used as a cathode for sodium rechargeable hybrid aqueous battery.

SEM allowed investigating morphology of the synthesized NMO and NMO-RGO composites (Fig. 2). It can be seen from Fig. 2a that the pristine NMO owns a needle-like morphology with the needles length of ~2 μm and diameter of ~100 nm. Insignificant agglomeration of these NMO needles could also be observed from the SEM picture. Fig. 2b shows a typical SEM image of a free-standing RGO film without addition of NMO. The curved and wrinkled surface of the sample indicates that the RGO film is built from stacked graphene sheets. The SEM images in Fig. 2c–h present the surface morphology of the NMO-RGO films. One can see that NMO is uniformly distributed on a well-developed flexible film, providing enhanced contact of NMO with the conductive graphene sheets, and improving the mechanical integrity of the composite. Such structural features and good contact of the components is crucial for the electrochemical performance improvement of the cathode. In the same time, it can be seen from the SEM images that a decrease in the graphene content within a series of the composites from NMO-RGO-3, NMO-RGO-2 to NMO-RGO-1 increases the NMO needles agglomeration. The thickness of the composite films was estimated by SEM imagining of their cross-section. The obtained images are presented in the insets of Fig. 2d,f and h. The edges of the films cross-sections display a well-compacted layer-by-layer stacking of the graphene sheets. The average thickness of the films is about 20–30 μm.

The distribution and sizes of NMO needles in the NMO-RGO films, the pristine NMO and NMO-RGO-2 composite were studied using TEM. It can be seen from Fig. 3a and Fig. 3c that the pristine NMO forms needle-like particles with a diameter about 50–100 nm and several μm in length. Some of the $Na_4Mn_9O_{18}$ needles agglomerate and form bundles, which could be due to the high temperature sintering during preparation of $Na_4Mn_9O_{18}$. The high-resolution TEM (HRTEM) image of $Na_4Mn_9O_{18}$ in Fig. 3e clearly exhibits the characteristic lattice fringes of $Na_4Mn_9O_{18}$. Fig. 3b and d present a typical TEM image of the NMO-RGO-2 composite, which corresponds with the SEM data, and shows the $Na_4Mn_9O_{18}$ needles uniformly anchored on the graphene sheets with wrinkled surface. There is no obvious agglomeration of $Na_4Mn_9O_{18}$ needles observed for this composite. In the same time, one can see that the dimensions of the $Na_4Mn_9O_{18}$ needles anchored on the graphene sheets are similar to that of the pristine $Na_4Mn_9O_{18}$. The HRTEM image in Fig. 3f was taken for the same sample as in Fig. 3d, and it clearly shows the lattice fringes of $Na_4Mn_9O_{18}$ surrounded by a graphene polycrystalline lattice. The SEM and TEM images and the XRD data in Fig. 1a confirm that the NMO-RGO composite films with the $Na_4Mn_9O_{18}$ needle-like nanoparticles anchored on RGO were successfully synthesized by a simple preparation method used in this work.

The electrochemical performance of the NMO-RGO-2 composite film as a cathode was examined in ReHAB by CV and galvanostatic cycling (charge-discharge) tests (Fig. 4). The CV curves of the free-standing NMO-RGO-2 electrode conducted at a scan rate of 0.1 mV s^{-1} are shown in Fig. 4a. It can be seen in all CV profiles that there is a pair of reduction and oxidation peaks at ~1.37 and ~1.55 V *vs.* Zn^{2+}/Zn, respectively, apparently indicating the one-step

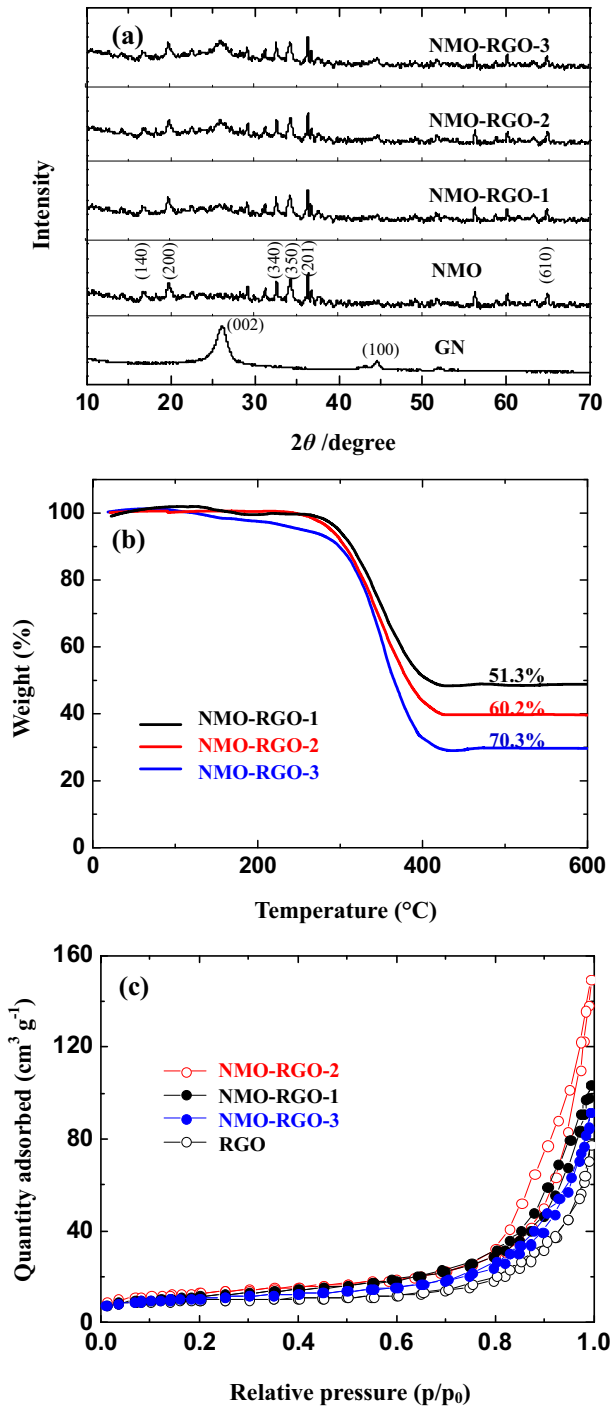

Fig. 1. (**a**) XRD patterns of the synthesized samples, (**b**) TGA data of NMO-RGO composites, (**c**) nitrogen adsorption/desorption isotherms of RGO and NMO-RGO composites.

sodium deintercalation/intercalation in the cathode. Graphene is electrochemically inactive within the investigated potential range [10,28]. The anodic peak at ~1.95 V can be assigned to the oxygen evolution reaction due to the water decomposition [9]. In the following cycles, NMO-RGO-2 exhibits a stable cyclability and electrochemical reversibility maintaining the redox peaks position/potential and the current. In order to avoid the side reaction of water decomposition, the cutoff potentials for galvanostatic discharge-charge of the test cells were restricted between 1.05 and 1.85 V *vs.* Zn^{2+}/Zn. The potential curves of the first three cycles of galvanostatic discharge-charge of the NMO-RGO-2 free-standing cathode film at 100 mA g^{-1} are shown in the Fig. 4b. The NMO-RGO-2 electrode shows one well-defined potential plateau at ~1.37 V and ~1.55 V in its discharge and charge curves, respectively, which corresponds well with the CV data above. The highest discharge capacity of 83 mAh g^{-1} was delivered at the first cycle. The corresponding charge capacity is 122 mAh g^{-1}, which corresponds to a coulombic efficiency of 68%. This low coulombic efficiency could be caused by the irreversible side reactions during the first charge process. Although the nature and mechanism of these reactions is unclear and will be further investigated in our following works, it could be suggested that there are the reactions involving both the solvent (water) and the electrolyte salts (mostly their anions), which lead to formation of a layer similar to the surface electrolyte interfaces (SEI) reported for lithium-ion batteries. This process could be reason of the performance stabilization upon the following cycles: by the third cycle, the coulombic efficiency of the cell increases to a high value close to 94%.

To further examine and compare the electrochemical performance of the NMO-RGO film electrodes with different RGO content, pristine NMO, NMO-RGO-1, NMO-RGO-2 and NMO-RGO-3 electrodes were investigated using a stepwise current rate increase experiment. As it is shown in Fig. 5a, the rate performance of the NMO-RGO electrodes is significantly improved compared with the pristine NMO electrode. Among all NMO-RGO electrodes, the NMO-RGO-2 film electrode exhibited the highest reversible capacity at high current densities and the best capacity recovery when the current density was decreased to 0.2 A g^{-1}. It can be seen that the NMO-RGO-2 film electrode delivers reversible capacities of 83, 43, 33, 24, 16 and 13 mAh g^{-1} at current densities of 0.1 A g^{-1}, 0.2 A g^{-1}, 0.5 A g^{-1}, 1 A g^{-1}, 2 A g^{-1} and 5 A g^{-1}, respectively. The cell recovers a capacity of about 31 mAh g^{-1} when the current density was decreased to the initial value of 0.2 A g^{-1}; the cell exhibits a capacity retention as high as 72%. For the pristine NMO and NMO-RGO-1 and NMO-RGO-3 composite electrodes, the reversible capacities are lower for 20–40 mAh g^{-1} than for the NMO-RGO-2 electrode within the studied current density range. For all the prepared electrodes, the coulombic efficiency of the NMO-RGO composites in sodium rechargeable hybrid aqueous batteries reaches abound 99% after a few initial cycles. Prolonged cycling abilities of the pristine NMO, NMO-RGO-1, NMO-RGO-2 and NMO-RGO-3 electrodes at 0.2 A g^{-1} are presented in Fig. 5a as well. One can see that all cathodes exhibit a stable cyclability. Among these electrodes, the NMO-RGO-2 electrode retains the highest reversible capacity of 29.4 mAh g^{-1} after 160 cycles. In contrast, the sodium rechargeable hybrid aqueous batteries with NMO, NMO-RGO-1, and NMO-RGO-3 cathodes deliver specific discharge capacities of only about 15.2 mAh g^{-1}, 21.4 mAh g^{-1} and 25.9 mAh g^{-1}, respectively. It was shown that the performance of the NMO-RGO film electrodes was remarkably improved by addition of graphene, which enhanced the composite electrodes conductivity. In the NMO-RGO composites, the NMO needles were exceedingly cross-connected by the graphene sheets, providing a fast ion/electron transfer pathways and short diffusion distances for the Na^+ transport. Excess of graphene in the composite film decreases the content of the electrochemically active $Na_4Mn_9O_{18}$. In the same time, deficiency of graphene results in insufficient electronic conductivity of the film. From the results of our studies, it was found that the NMO-RGO-2 electrode with 60 wt% of graphene could be considered as the most optimized from the series of the composites prepared in this work, exhibiting the best electrochemical properties.

For further exploration of influence of the film electrode composition on charge transfer behavior and conductivity of the system, the EIS measurements for the pristine NMO and NMO-RGO

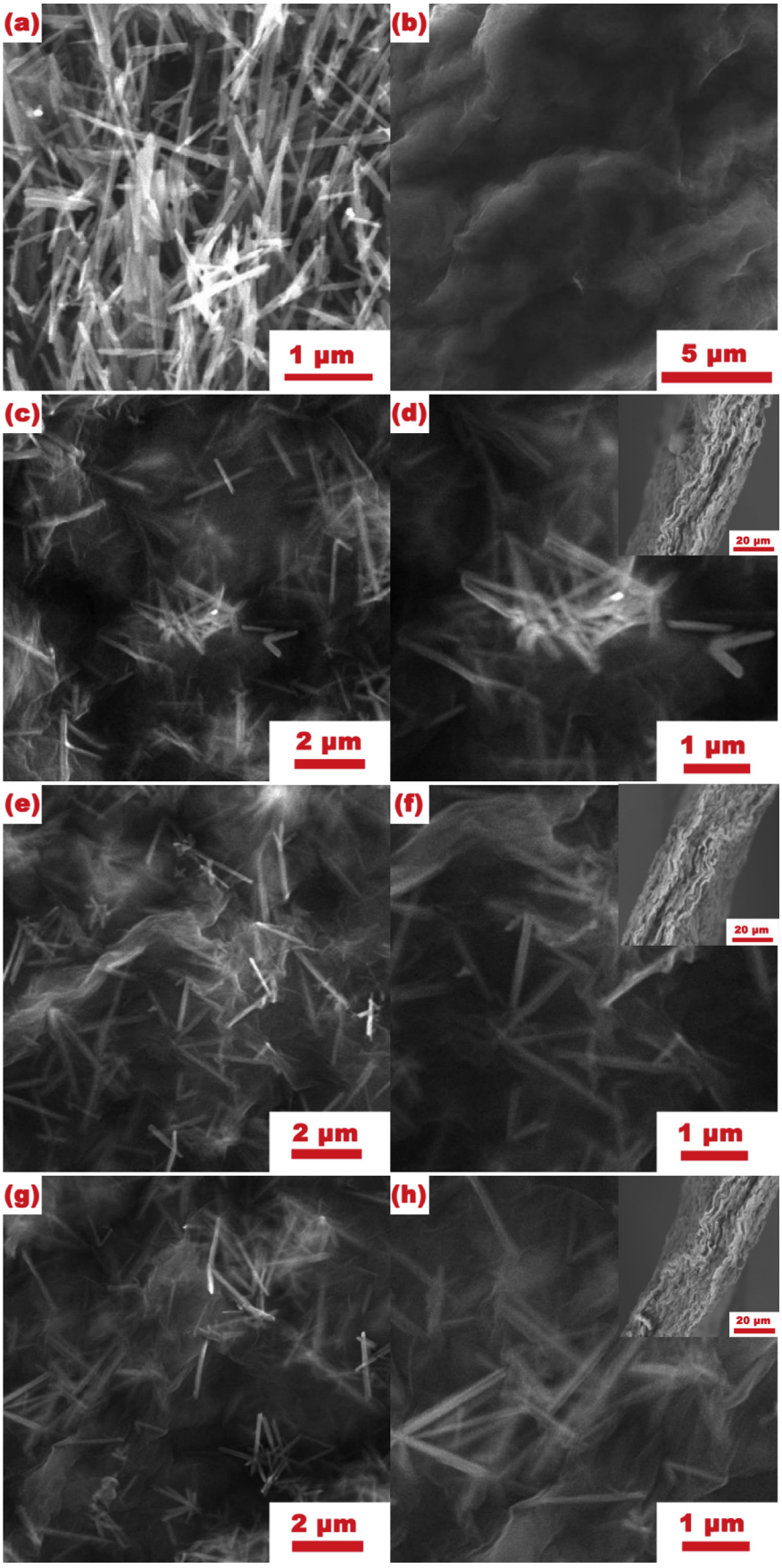

Fig. 2. SEM images of (**a**) NMO, (**b**) RGO, (**c**, **d**) NMO-RGO-1, (**e**, **f**) NMO-RGO-2, and (**g**, **h**) NMO-RGO-3.

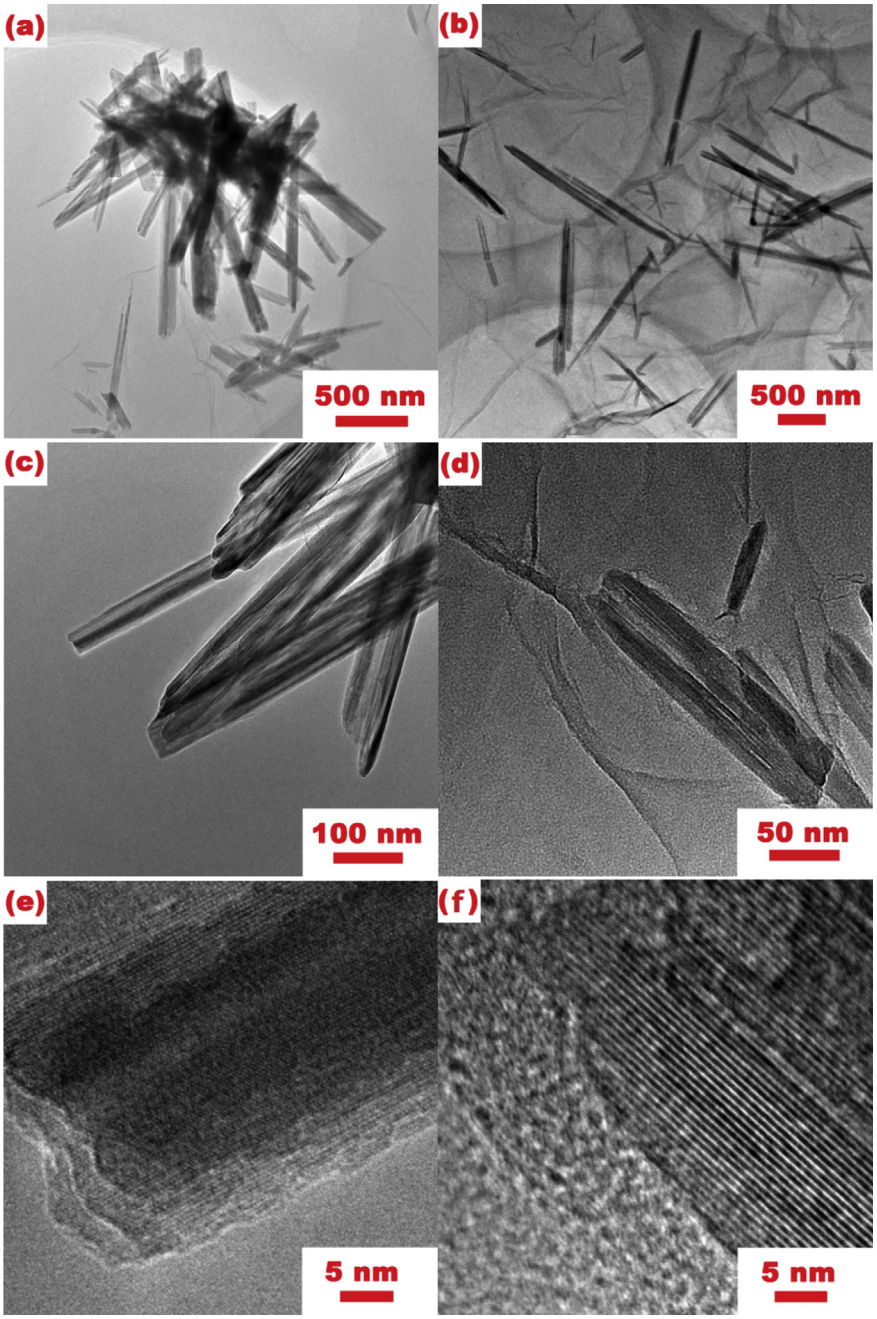

Fig. 3. TEM images of (**a**, **c**, **e**) pristine NMO and (**b**, **d**, **f**) NMO-RGO-2 composite.

composite electrodes were carried out (Fig. 5b). It should be noted that the electrodes and cells were constructed to maintain as much as possible similar dimensions and geometry. This measure could allow for comparative analysis of the tendencies in the EIS of the systems, and reduce the errors of such comparative analysis. A semicircle at the high-to-medium frequency region and a straight line at the low frequency part of EIS compose the impedance plots of the electrodes in their discharged states. The Nyquist plots could be fitted with the equivalent circuit as shown in the insert in Fig. 5b. The intercept in the high frequency region corresponds to the ohmic resistance (R_Ω), which combines total resistance of the electrolyte, separator, and electrical contacts. The semicircle is mainly attributed to the constant phase capacitance (*CPE*) of SEI film and the charge-transfer resistance (R_{ct}) at the electrode/electrolyte interface, while a straight line is commonly attributed to the 'Warburg impedance' (W) corresponded with the Na^+ or Li^+ diffusion in the bulk of electrode [29]. As a general tendency observed from the EIS data, the R_{ct} of the electrodes reduces when graphene is introduced into the composite electrode. In detail, the R_{ct} value for the NMO-RGO-1, NMO-RGO-2 and NMO-RGO-3 electrodes are about 13.8 Ω, 18.1 Ω and 20.2 Ω respectively, which are apparently lower than that of the pristine NMO electrode (38.3 Ω). This enhancement resulted from the graphene addition along with structuring the system and creating the conditions to buffer the volume changes of $Na_4Mn_9O_{18}$ upon cycling, leads to a remarkably enhanced performance of the NMO-RGO composites compared with the pristine NMO, and favors the mechanical integrity of the composite film electrode. Furthermore, it should be noted that the

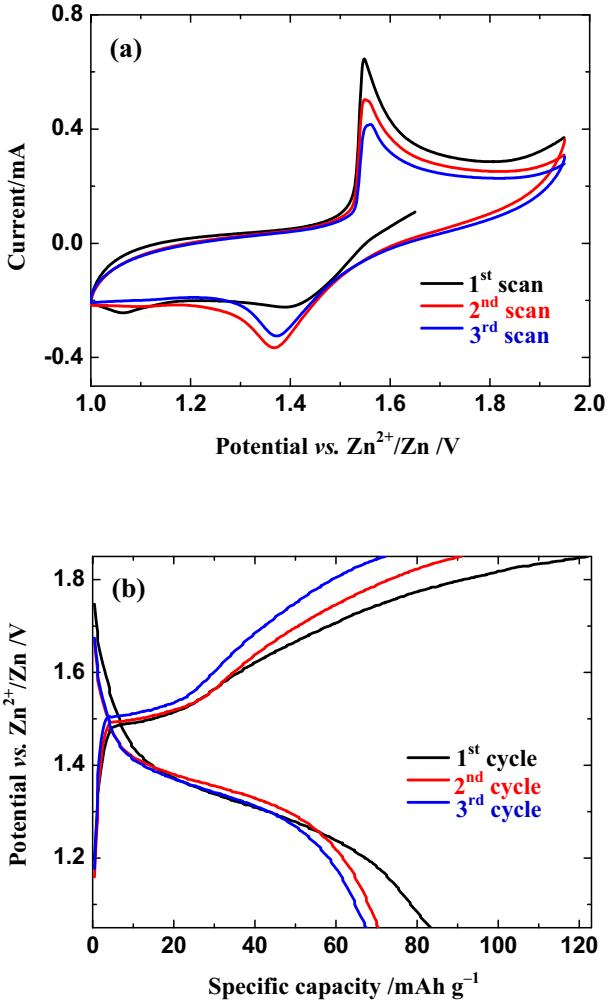

Fig. 4. (**a**) CV curves of a cell with NMO-RGO-2 electrode, (**b**) charge–discharge profiles of a cell with NMO-RGO-2 electrode at 100 mA g^{-1}.

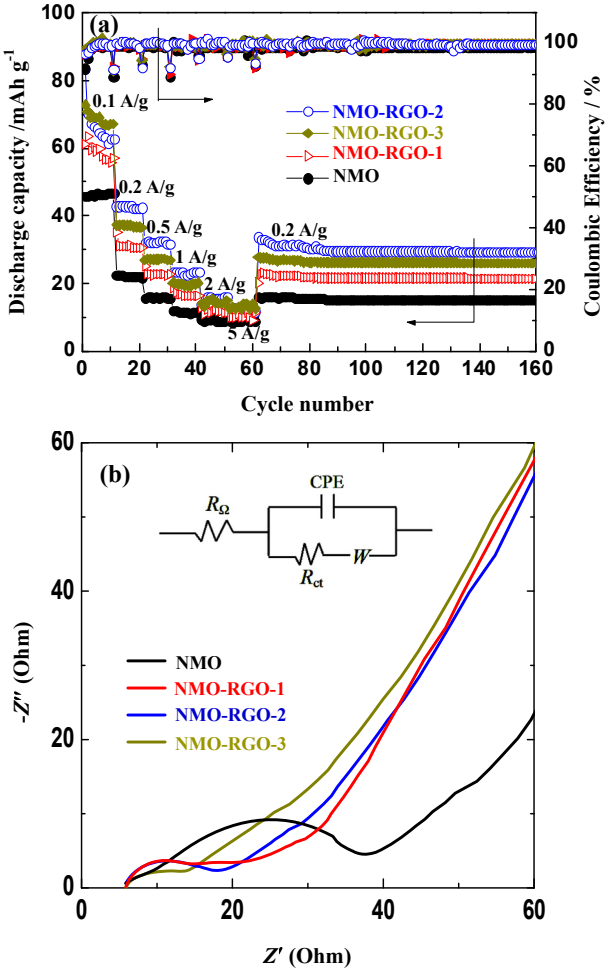

Fig. 5. (**a**) Cycle performance and (**b**) EIS of cells with NMO and NMO-RGO electrodes.

NMO-RGO-2 electrode having a medium charge-transfer resistance among three RGO electrodes, exhibits the best electrochemical performance as shown in Fig. 5a. This enhancement could be attributed to the synergetic effect coming from NMO particles and RGO. For the NMO-RGO-2 composite, the NMO needle-like particles could be uniformly anchored onto the conductive RGO matrix (Fig. 2e and f), and RGO support also plays a decisive role in alleviating the volume expansion and preventing the aggregation of NMO particles. When the RGO loading increases to 70 wt% (NMO-RGO-3), excess of graphene in the composite film decreases the content of the electrochemically active $Na_4Mn_9O_{18}$. As the RGO loading decreases to 51 wt% (NMO-RGO-1), the conductivity and synergetic effects between NMO particles and the RGO support become weak, resulting in a limited ability to store lithium.

4. Conclusions

Flexible free-standing $Na_4Mn_9O_{18}$-reduced graphene oxide hybrid films were successfully prepared via a simple vacuum filtration followed by a reduction step. This inexpensive preparation technique results in a uniform distribution of the $Na_4Mn_9O_{18}$ particles over the RGO matrix, and provides a convenient way of controlling its content. The NMO-RGO composite films exhibited remarkably enhanced electrochemical performance as a cathode for aqueous sodium cells compared with the pristine $Na_4Mn_9O_{18}$, demonstrating a great potential of this self-standing composite film as a cathode for rechargeable aqueous batteries. Among the composite films with different RGO content, the one with 60 wt% exhibited the best electrochemical properties. The smaller charge transfer resistance and an enhanced electronic conductivity were found to be the main factors positively affecting the electrochemical performance of the electrodes. Furthermore, a structure formed due to the graphene addition, i.e. needle-like $Na_4Mn_9O_{18}$ homogeneously distributed and anchored on the RGO matrix, could significantly reduce the stresses in the system caused by the volume changes of $Na_4Mn_9O_{18}$ upon cycling, remarkably improving cyclability of the electrodes. To best of our knowledge, this work is the first report on the use of the $Na_4Mn_9O_{18}$-RGO original composite films as a cathode in ReHABs.

Acknowledgments

This work was supported by Natural Science Fund of Education Department of Shaanxi Provincial Government (Grant No. 16JK018), Natural Science Fund and Subject Merging Fund of Ankang University for high-level talents (Grant Nos. 2016AYQDZR05 and 2017AYJC01), the targeted program 0115CK03029 ((NU-Berkeley strategic initiative in warm-dense matter, advanced materials and energy sources for 2014-2018) and grant 3756/ГФ4-1 from the Ministry of Education and Science of the Republic of Kazakhstan.

YGZ acknowledges the financial support by the Program for the Outstanding Talents of Guangdong sailing plan, Human Resources and Social Security of Guangdong Province.

References

[1] Y. Zhang, Y. Li, H. Li, Y. Zhao, F. Yin, Electrochemical performance of carbon-encapsulated Fe_3O_4 nanoparticles in lithium-ion batteries: morphology and particle size effects, Electrochim. Acta 216 (2016) 475.

[2] H. Li, Y. Wei, Y. Zhang, C. Zhang, G. Wang, Y. Zhao, F. Yin, Z. Bakenov, In situ sol-gel synthesis of ultrafine ZnO nanocrystals anchored on graphene as anode material for lithium-ion batteries, Ceram. Int. 42 (2016) 12371.

[3] P.G. Bruce, S.A. Freunberger, L.J. Hardwick, J.M. Tarascon, Li-O_2 and Li-S batteries with high energy storage, Nat. Mater. 11 (2012) 19.

[4] R.J. Clément, P.G. Bruce, C.P. Grey, Review-manganese-based P2-type transition metal oxides as sodium-ion battery cathode materials, J. Electrochem. Soc. A162 (2015) 2589.

[5] M.H. Han, E. Gonzalo, G. Singh, T. Rojo, A comprehensive review of sodium layered oxides: powerful cathodes for Na-ion batteries, Energy Environ. Sci. 8 (2015) 81.

[6] L. Suo, O. Borodin, T. Gao, M. Olguin, J. Ho, X. Fan, C. Luo, C. Wang, K. Xu, "Water-in-salt" electrolyte enables high-voltage aqueous lithium-ion chemistries, Science 350 (2015) 938.

[7] W. Wu, S. Shanbhag, A. Wise, J. Chang, A. Rutt, J.F. Whitacre, High performance TiP_2O_7 based intercalation negative electrode for aqueous lithium-ion batteries via a facile synthetic route, J. Electrochem. Soc. A162 (2015) 1921.

[8] X. Zeng, Q. Liu, M. Chen, L. Leng, T. Shu, L. Du, H. Song, S. Liao, Electrochemical behavior of spherical $LiFePO_4$/C nanomaterial in aqueous electrolyte, and novel aqueous rechargeable lithium battery with $LiFePO_4$/C anode, Electrochim. Acta 177 (2015) 277.

[9] J. Yan, J. Wang, H. Liu, Z. Bakenov, D. Gosselink, P. Chen, Rechargeable hybrid aqueous batteries, J. Power Sources 216 (2012) 222.

[10] G. Yuan, J. Bai, T.N.L. Doan, Synthesis and electrochemical properties of $LiFePO_4$/graphene composite as a novel cathode material for rechargeable hybrid aqueous battery, Mater. Lett. 158 (2015) 248.

[11] Q.T. Qu, Y. Shi, S. Tian, Y.H. Chen, Y.P. Wu, R. Holze, A new cheap asymmetric aqueous supercapacitor: activated carbon//$NaMnO_2$, J. Power Sources 194 (2009) 1222.

[12] L. Ke, J. Dong, B. Lin, T. Yu, H. Wang, S. Zhang, C. Deng, A $NaV_3(PO_4)_3$@C hierarchical nanofiber in high alignment: exploring a novel high-performance anode for aqueous rechargeable sodium batteries, Nanoscale 9 (2017) 4183.

[13] B.H. Zhang, Y. Liu, X.W. Wu, Y.Q. Yang, Z. Chang, Z.B. Wen, Y.P. Wu, An aqueous rechargeable battery based on zinc anode and Na(0.95)MnO2, Chem. Commun. 50 (2014) 1209.

[14] K. Park, B.C. Yu, J.B. Goodenough, Electrochemical and chemical properties of Na_2NiO_2 as a cathode additive for a rechargeable sodium battery, Chem. Mater. 27 (2015) 6682.

[15] Z. Hou, X. Li, J. Liang, Y. Zhu, Y. Qian, An aqueous rechargeable sodium ion battery based on a $NaMnO_2$-$NaTi_2(PO_4)_3$ hybrid system for stationary energy storage, J. Mater. Chem. A 3 (2015) 1400.

[16] I. Hasa, R. Verrelli, J. Hassoun, Transition metal oxide-carbon composites as conversion anodes for sodium-ion battery, Electrochim. Acta 173 (2015) 613.

[17] X. Rui, W. Sun, C. Wu, Y. Yu, Q. Yan, An advanced sodium-ion battery composed of carbon coated $Na_3V_2(PO_4)_3$ in a porous graphene network, Adv. Mater. 27 (2015) 6670.

[18] M. Moradi, Z. Li, J. Qi, W. Xing, K. Xiang, Y.M. Chiang, A.M. Belcher, Improving the capacity of sodium ion battery using a virus-templated nanostructured composite cathode, Nano Lett. 15 (2015) 2917.

[19] Y. Meng, T. Yu, S. Zhang, C. Deng, Top-down synthesis of muscle-inspired alluaudite $Na_{2+2x}Fe_{2-x}(SO_4)_3$/SWNT spindle as a high-rate and high-potential cathode for sodium-ion batteries, J. Mater. Chem. A 4 (2016) 1624.

[20] S. Zhang, C. Deng, F.L. Liu, Q. Wu, M. Zhang, F.L. Meng, H. Gao, Impacts of in situ carbon coating on the structural, morphological and electrochemical characteristics of Li_2MnSiO_4 prepared by a citric acid assisted sol–gel method, J. Electroanal. Chem. 689 (2013) 88.

[21] K. Cao, L. Jiao, Y. Liu, H. Liu, Y. Wang, H. Yuan, Ultra-high capacity lithium-ion batteries with hierarchical CoO nanowire clusters as binder free electrodes, Adv. Funct. Mater. 25 (2015) 1082.

[22] X. Dong, L. Chen, X. Su, Y. Wang, Y. Xia, Flexible aqueous lithium-ion battery with high safety and large volumetric energy density, Angew. Chem. Int. Ed. 55 (2016) 7474.

[23] Y. Zhao, F. Yin, Y. Zhang, C. Zhang, A. Mentbayeva, N. Umirov, H. Xie, Z. Bakenov, A free-standing sulfur/nitrogen doped carbon nanotube electrode for high performance lithium/sulfur batteries, Nanoscale Res. Lett. 10 (2015) 450.

[24] K. Rana, S.D. Kim, J.H. Ahn, Additive-free thick graphene film as an anode material for flexible lithium-ion batteries, Nanoscale 7 (2015) 7065.

[25] H. Tang, Y.J. Zhang, Q.Q. Xiong, J.D. Cheng, Q. Zhang, X.L. Wang, C.D. Gu, J.P. Tu, Self-assembly silicon/porous reduced graphene oxide composite film as a binder-free and flexible anode for lithium-ion batteries, Electrochim. Acta 156 (2015) 86.

[26] Y. Zhang, Y. Wei, H. Li, Y. Zhao, F. Yin, Simple fabrication of free-standing ZnO/graphene/carbon nanotube composite anode for lithium-ion batteries, Mater. Lett. 184 (2016) 235.

[27] J. Zhao, S. Pei, W. Ren, L. Gao, H.M. Cheng, Efficient preparation of large-area graphene oxide sheets for transparent conductive films, ACS Nano 4 (2010) 5245.

[28] G. Yuan, J. Bai, T.N. Doan, P. Chen, Synthesis and electrochemical investigation of nanosized $LiMn_2O_4$ as cathode material for rechargeable hybrid aqueous batteries, Mater. Lett. 137 (2014) 311.

[29] D. Aurbach, Electrode-solution interactions in Li-ion batteries: a short summary and new insights, J. Power Sources 119 (2003) 497.